PHYSICAL REVIEW B **104**, 075134 (2021)

Coexistence of ferromagnetism and topology by charge carrier engineering in the intrinsic magnetic topological insulator $MnBi_4Te_7$

Bo Chen,[1,2] Dinghui Wang,[1] Zhicheng Jiang,[3] Bo Zhang,[4] Shengtao Cui,[4] Jingwen Guo,[1,2] Hangkai Xie,[1,2]
Yong Zhang,[1,2] Muhammad Naveed,[1,2] Yu Du,[1,2] Xuefeng Wang,[2,5] Haijun Zhang,[1]
Fucong Fei,[1,2,*] Dawei Shen,[3,†] Zhe Sun,[4,‡] and Fengqi Song[1,2]
[1]*National Laboratory of Solid State Microstructures, Collaborative Innovation Center of Advanced Microstructures, and College of Physics, Nanjing University, Nanjing 210093, China*
[2]*Atomic Manufacture Institute (AMI), Nanjing 211805, China*
[3]*Center for Excellence in Superconducting Electronics, State Key Laboratory of Functional Materials for Informatics, Shanghai Institute of Microsystem and Information Technology, Chinese Academy of Sciences, Shanghai 200050, China*
[4]*National Synchrotron Radiation Laboratory, University of Science and Technology of China, 230029 Hefei, China*
[5]*School of Electronic Science and Engineering, Nanjing University, Nanjing 210093, China*

(Received 6 February 2021; accepted 29 July 2021; published 18 August 2021)

Intrinsic magnetic topological insulators (MTIs) $MnBi_2Te_4$ and $MnBi_2Te_4/(Bi_2Te_3)_n$ are expected to realize the high-temperature quantum anomalous Hall effect and dissipationless electrical transport. However, there is still a lack of ideal MTI candidates with magnetic ordering of the ferromagnetic (FM) ground state. Here, we show a MTI sample of $Mn(Bi_{0.7}Sb_{0.3})_4Te_7$ which holds the coexistence of a FM behavior state and topological nontriviality. The dramatic modulation of the magnetism is induced by a charge carrier engineering process via the Sb substitution in the $MnBi_4Te_7$ matrix with antiferromagnetic ordering. The evolution of magnetism in $Mn(Bi_{1-x}Sb_x)_4Te_7$ is systematically investigated by our magnetic measurements and theoretical calculations. The clear topological surface states of the FM sample of $Mn(Bi_{0.7}Sb_{0.3})_4Te_7$ are further verified by angle-resolved photoemission spectroscopy. The demonstration of the intrinsic FM-MTI of $Mn(Bi_{0.7}Sb_{0.3})_4Te_7$ in this paper sheds light on further material optimization of intrinsic MTIs and paves the way for further studies to clarify the relationships between topology, magnetism, and charge carriers in topological materials.

DOI: 10.1103/PhysRevB.104.075134

I. INTRODUCTION

Topological insulators, combined with magnetism, can host various intriguing phenomena, such as quantum anomalous Hall effect (QAHE), topological electromagnetic effect, axion state, and so on [1–7]. However, due to the confinement of the material candidates, research on magnetic topological insulators (MTIs) is limited to the magnetic doped topological insulators or magnetic proximity in heterostructures [8–11]. In recent years, intrinsic MTIs $MnBi_2Te_4$ and a series of $MnBi_2Te_4/(Bi_2Te_3)_n$ materials have sprung up, in which spontaneous magnetization derives from the internal manganese atoms instead of external impurities [12–19]. Unfortunately, due to the compensated antiferromagnetic (AFM) ground state, the magnetization intensity of $MnBi_2Te_4$ is rather weak under the zero field. $MnBi_2Te_4/(Bi_2Te_3)_n$ series samples can significantly reduce the interlayer AFM exchange interaction by intercalated Bi_2Te_3 quintuple layers [20,21], but the AFM ground state still possesses lower energy than the ferromagnetic (FM) state, and a small magnetic field is still required to align the opposite magnetic moments. Furthermore, in all these recent known intrinsic MTI candidates, the ineluctable antisite defects between the manganese and bismuth atoms can induce heavy n-type trivial bulk carriers [14,22], covering the transport of the novel chiral edge state. Up to now, a Chern insulator state can only be realized in $MnBi_2Te_4$ thin films with high magnetic field up to 6 T or near zero field with high bias voltage (∼200 V) [23–25]. Such a high magnetic field and a large bias voltage limit the steerability of the Chern insulator state in $MnBi_2Te_4$ and obstruct further applications. In $MnBi_2Te_4$, Sb substitution of Bi sites can neutralize the excess bulk carrier efficiently, while the AFM state remains robust [26,27]. However, in the case of $MnBi_4Te_7$, the comparable FM-AFM energy difference offers an opportunity to modify the magnetic ground state with a charge carrier engineering process via nonmagnetic elemental doping.

In this paper, we grow a series of single crystals of $Mn(Bi_{1-x}Sb_x)_4Te_7$ with $x = 0.15$–0.46. Angle-resolved photoemission spectroscopy (ARPES), magnetic, and electrical transport measurements are conducted to explore the influence of Sb substitution of $Mn(Bi_{1-x}Sb_x)_4Te_7$. Through nonmagnetic element Sb doping, the AFM ground state evolves to a FM state at $x = 0.3$, and then returns to an AFM state at $x = 0.36$, indicating an unexpected FM behavior region in the middle. According to theoretical calculations, the energy difference between FM and AFM in the $MnBi_4Te_7$ family is

---

[*] feifucong@nju.edu.cn

[†] dwshen@mail.sim.ac.cn

[‡] zsun@ustc.edu.cn

only ~0.2 meV, indicating that the magnetic ordering could be engineered by external conditions. The calculations also reveal a narrow negative region of the energy difference between the FM and AFM near $x = 0.3$, which may derive from the accidental emergence of band filling at the Van Hove singularity (VHS), qualitatively agreeing with the trend displayed in our experimental results. Furthermore, according to the electrical transport, we find that, like the case of $MnBi_2Te_4$ [26–28], Sb doping is also effective to modulate the carrier density. Specifically, the heavy n-type bulk carriers in pure $MnBi_4Te_7$ are significantly suppressed by Sb doping, and an $n - p$ transition occurs between $x = 0.36$ and 0.4. One may notice that the charge neutrality point of Sb-doped $MnBi_4Te_7$ is close to the FM behavior state region. From the ARPES measurement, the clear surface Dirac cone of Bi_2Te_3 termination corroborates the robust topological characteristic of $Mn(Bi_{0.7}Sb_{0.3})_4Te_7$. This paper demonstrates the facile engineering of both magnetism and the charge carriers of $MnBi_4Te_7$ by Sb doping. $Mn(Bi_{1-x}Sb_x)_4Te_7$ with $x \sim 0.3$ is a promising candidate of MTI displaying the FM behavior state and low bulk carrier concentration. This paper provides a prospective avenue to mediate the magnetism by carrier densities, for approaching other exotic phenomena in topological materials.

II. EXPERIMENTAL DETAILS

High-quality $Mn(Bi_{1-x}Sb_x)_4Te_7$ crystals can be synthesized by the self-flux method. For pure $MnBi_4Te_7$, the raw materials of Mn, Bi, and Te were mixed with a stoichiometric ratio of $MnTe{:}Bi_2Te_3$ of 1:7 and put in an alumina crucible, which was further sealed inside a clean quartz ampule under a high-vacuum environment. The ampule was then transferred into a high-temperature furnace and heated up to 1223 K, over 1 d. After sustaining it at 1223 K for 1 d, the ampule was cooled down to 848 K in 2 d and then centrifuged immediately at the same temperature. For the samples of Sb doping, different amounts of Sb were used to substitute for Bi. Due to Sb substitution, the temperatures for centrifuge increased slightly with the doping concentration. It is notable that the melting point difference between $Mn(Bi_{1-x}Sb_x)_4Te_7$ and $(Bi_{1-x}Sb_x)_2Te_3$ was tiny. The real temperatures of every furnace require special checks and calibration before crystal growth.

ARPES experiments were performed at the BL03U beamline at the Shanghai Synchrotron Radiation Facility and the BL13U beamline at the Hefei National Synchrotron Radiation Laboratory. All samples were cleaved and measured in an ultrahigh vacuum $<10^{-10}$ Torr. The photon energies were selected ranging from 7.25 to 23 eV.

The magnetic and electrical resistivity were measured using a physical property measurement system (Quantum Design PPMS-14T). The lowest temperature and highest magnetic field were 2 K and 14 T, respectively. For magnetic measurement, a vibrating sample magnetometer with the standard copper sample holders was used to obtain the magnetization signals of the sample. For electrical transport, standard Hall bar contacts were fabricated using silver paste or indium pressing on the cleaved sample surface.

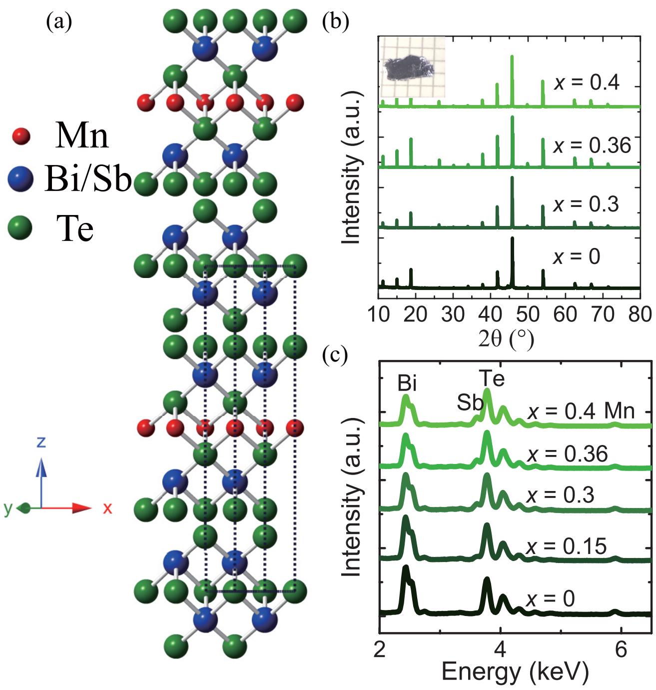

FIG. 1. Characterization of $Mn(Bi_{1-x}Sb_x)_4Te_7$. (a) Crystal structure of $Mn(Bi_{1-x}Sb_x)_4Te_7$. (b) Single crystal x-ray diffraction patterns of the four samples. Inset: Optical images of the as-grown sample. (c) Energy dispersive spectra after normalized with the intensity of the Te element. The curves are offset for clarity.

The first-principles calculations were carried out in the framework of the generalized gradient approximation functional of the density functional theory through employing the Vienna *ab initio* Simulation Package (VASP) with projector augmented wave pseudopotentials [29,30]. The cutoff energy was 500 eV, and a $16 \times 16 \times 4$ k-point grid using Monkhorst-Pack method was used in self-consistent calculation. Spin-orbit coupling (SOC) was included in calculations. An effective $U_{\mathrm{eff}} = 3$ eV was used for Mn 3d orbitals.

III. RESULTS AND DISCUSSION

$Mn(Bi_{1-x}Sb_x)_4Te_7$ is a layered rhombohedral material with the space group $P\bar{3}m1$ (164) [31–34]. $Mn(Bi_{1-x}Sb_x)_4Te_7$ superlattice stacks along the c axis through the weak van der Waals forces, as schematically shown in Fig. 1(a). There are two various cleavage planes with independent Dirac cones as reported before: $Mn(Bi, Sb)_2Te_4$ SL and $(Bi, Sb)_2Te_3$ quintuple layer [21,33,35–38]. We synthesized the crystals of $Mn(Bi_{1-x}Sb_x)_4Te_7$ by the self-flux method to obtain lustrous flakes with average size $\sim 3 \times 3$ mm^2. The inset of Fig. 1(b) presents the photograph image of the as-grown shiny $Mn(Bi_{1-x}Sb_x)_4Te_7$ crystals. Single crystal x-ray diffraction (XRD) patterns show prominent peaks labeling (00n) Miller indexes in Fig. 1(b). The refined value of the c axis is nearly at ~24 Å with the tiny change at different doping ratio, indicating the similar structure constants and identical layered-crystal structure of all samples. Figure 1(c) displays the energy dispersive spectra (EDS) which shows the stoichiometric ratio of Mn:(Bi + Sb):Te is about 1:4:7.

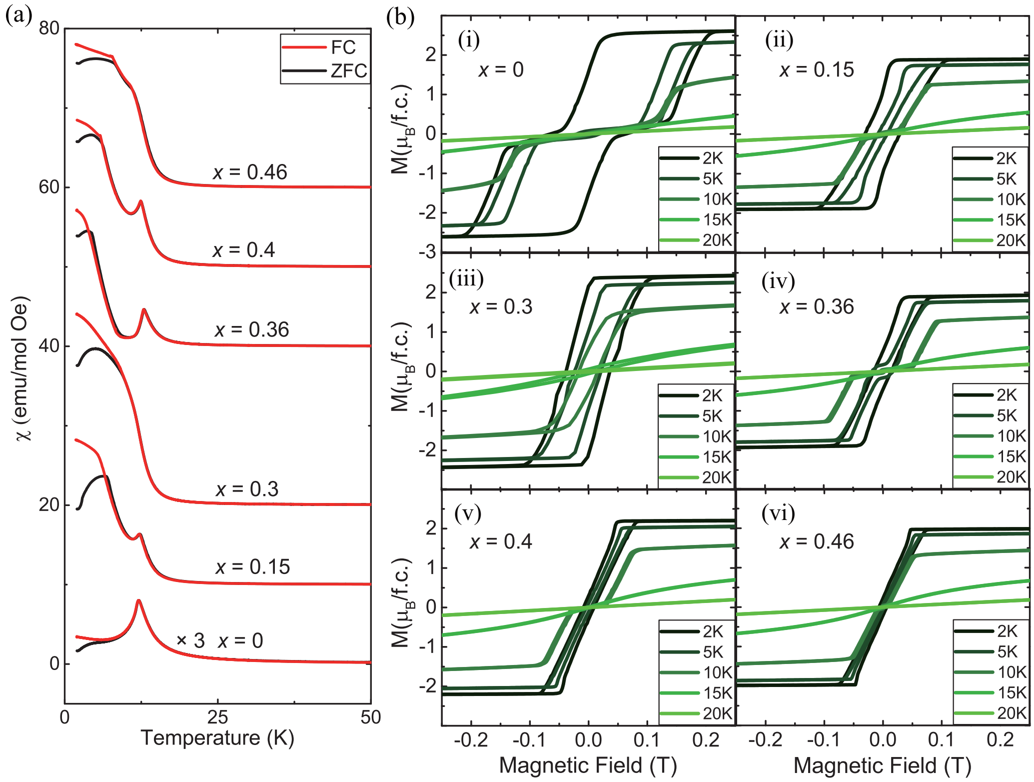

FIG. 2. Magnetism measurement of Mn(Bi$_{1-x}$Sb$_x$)$_4$Te$_7$ under H//c H // c. (a) Field cooling (FC)-zero field cooling (ZFC) curves of the six samples. The curves are offset for clarity. (b) The magnetic field dependence of the magnetization from 2 to 20 K.

The relative intensities of Bi at 3.8 keV and Sb at 3.6 keV evolve as expected after normalizing the counts with the Te peaks, indicating the valid substitution of the two elements. The x value of each sample is determined by EDS with the uncertainties <2%, which is a little bit higher than the nominal ratio with the proportion of raw materials. Both the XRD and EDS results demonstrate the favorable crystallinity and the precise molar ratio control in Mn(Bi$_{1-x}$Sb$_x$)$_4$Te$_7$.

To explore the magnetic variation in Mn(Bi$_{1-x}$Sb$_x$)$_4$Te$_7$ samples, we conducted the magnetic measurement of the field cooling (FC) and zero-field cooling (ZFC) processes from 300 to 2 K by vibrating sample magnetometer. The magnetic field was applied perpendicular to the sample cleaving surfaces with the magnitude of 500 Oe. In pure MnBi$_4$Te$_7$, the FC-ZFC curves show the expected AFM peaks at 13 K, and the overlapped ones diverge at lower temperature (∼5 K), consistent with the previous results [36,39]. The magnetic field dependence of the magnetization curves exhibit the zigzag shape at 2 K, and the hysteresis loop divides into two jump points deviating from the zero field at 10 K. Compared with MnBi$_2$Te$_4$ (∼7 T) [14,22], the saturation field of the FM region in MnBi$_4$Te$_7$, < 0.3 Tesla, is much smaller. However, as shown in Fig. 2(a), the FC-ZFC curves show typical AFM order with a kink feature at the Néel temperature (∼13 K) for the $x = 0$ sample. In addition, when $T = 5$ and 10 K, one can clearly see two separate loops antisymmetrically located at a certain positive and negative magnetic field in Fig. 2(b)(i), which correspond to the critical field of the spin-slip transition, i.e., a magnetic transition from AFM to FM when applying external magnetic fields. Thus, the magnetic ground state of pure MnBi$_4$Te$_7$ is AFM. The hysteresis of the spin-slip process becomes larger under lower temperatures, and finally, the two antisymmetrical loops merge, forming a big zigzag-shaped loop at 2 K. One may say that pure MnBi$_4$Te$_7$ samples are FM-like because there is a single big loop in the M-H curve <2 K. However, we need to emphasize this FM-like state at 2 K is a metastable state, and it can only be preserved when temperature is too low to overcome the energy barrier of the spin-flip transition to the AFM state [40]. When increasing the temperatures, the thermal fluctuation is strong enough to overcome the spin-flip transition barrier; thus, the samples tend to form the AFM order which is more stable than the FM order. Therefore, we say that the magnetic ground state in pure MnBi$_4$Te$_7$ is still AFM.

Due to Bi$_2$Te$_3$ intercalation which enlarges the distance between the neighboring MnBi$_2$Te$_4$ SL, the energy difference between the FM and AFM is relatively small in MnBi$_4$Te$_7$ [20,21,40]. Weak interlayer AFM coupling paves the way for the facile magnetic modulation by various approaches. For example, when substituting Bi with the nonmagnetic Sb element, the AFM ground state can be modulated without introducing the undesired magnetic impurities. From the FC-ZFC curves of the doped samples [Fig. 2(a)], the magnitude of the divergence at the lower temperature (∼5 K) rises and exceeds the value of the AFM transition point of 13 K, displaying the noticeable enhancement of the FM ingredient compared with the matrix. Most importantly, the peaks at ∼13 K in the FC-ZFC curves caused by the AFM magnetic transition vanish in Mn(Bi$_{0.7}$Sb$_{0.3}$)$_4$Te$_7$, and FC-ZFC curves diverge directly <13 K, demonstrating the typical signature of forming the FM ordering. Along with x increasing continuously, the signal of the FM behavior state disappears at $x = 0.36$ and 0.4 again, showing the recovery of the AFM ground state.

To further verify the magnetic ordering and the evolution of the magnetic ground state of the samples with various doping contents, the field-dependent magnetization curves (M-H) of the doped samples are displayed in Fig. 2(b). One can clearly see that the coercive field of the hysteresis loop decreases monotonically with increasing Sb concentration. However, the FM sample of $\mathrm{Mn(Bi_{0.7}Sb_{0.3})_4Te_7}$ is an exception, holding a significantly larger coercive field than that of $x = 0.15$. Further discussion on this sample is shown below. Note that the feature of zigzag-shaped hysteresis loops at 2 K [Fig. 2(b)(i)] evolves to the inclined rectangle-shaped loops located at zero field [Fig. 2(b)(ii)] in $\mathrm{Mn(Bi_{0.85}Sb_{0.15})_4Te_7}$. However, at 10 K, the hysteresis loop of this sample still splits and evolves into two small symmetric loops. This kind of behavior indicates the recovered domination of the AFM ground state and the FM-like properties at low temperature. It is believed to be held by a metastable magnetic state protected by the energy barrier during FM-AFM transition [40]. In $\mathrm{Mn(Bi_{0.7}Sb_{0.3})_4Te_7}$, the hysteresis behavior at 2 K displays a single loop located at zero field, like the ones in the samples of $x = 0.15$ and 0.36 at 2 K. However, when increasing the temperature, the hysteresis loop does not split into two loops with zigzag-shaped M-H curve. Instead, it simply shrinks and is always pinned at the zero field, which is distinct from the split ones of those AFM samples discussed above. This kind of hysteresis behavior demonstrates a typical FM ordering in the $\mathrm{Mn(Bi_{0.7}Sb_{0.3})_4Te_7}$ sample, consistent with the FC-ZFC behavior discussed above. We also grew more batches of crystals with $x = 0.3$ (Fig. S1 in the Supplemental Material [41]). All samples display the typical λ shaped FC-ZFC curves and the FM hysteresis loops near the zero field, which confirms the reproducibility of the FM behavior state in $\mathrm{Mn(Bi_{0.7}Sb_{0.3})_4Te_7}$. In addition, due to the distinct magnetic ordering, the coercive field in this sample is anomalously large compared with other samples [see Fig. 4(d)]. When x extends to 0.36 and 0.4, one can discover that the AFM state reoccurs because of the AFM transition peak (~13 K) in the FC-ZFC curves [Fig. 2(a)] and the split hysteresis loop in the M-H curves [Figs. 2(b)(iv) and 2(b)(v)]. We also notice that, when x increases to 0.46, the peak ~13 K shows noticeable decrease as compared with those of $x = 0.36$ and 0.4. When $x = 0.46$, the coercive field is quite small, and the AFM characteristic with the split loops is unambiguous. It seems that the sample of $x = 0.46$ probably shows exotic ferrimagnetism, which could be attributed to the weaker magnetism due to the excessive doping content.

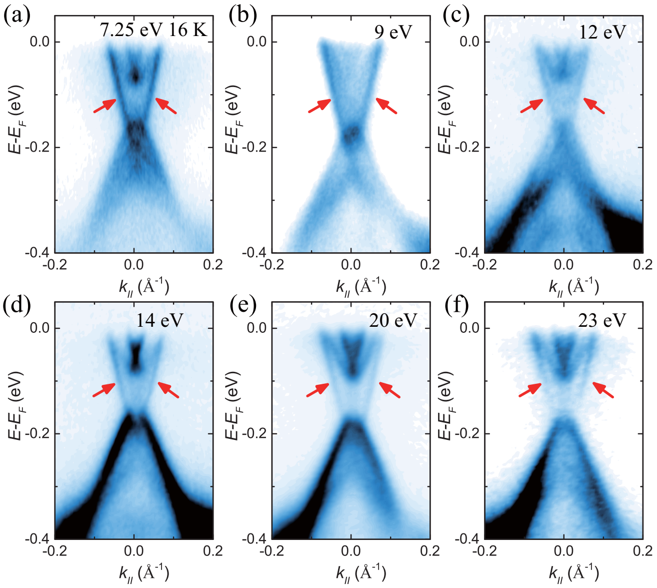

FIG. 3. Angle-resolved photoemission spectroscopy (ARPES) images of $\mathrm{Mn(Bi_{1-x}Sb_x)_4Te_7}$ at $x = 0.3$. (a)–(f) ARPES measurement at the photon energies from 7.2 to 23 eV. The topological surface states are marked by the red arrows.

We feel excited to accidentally discover the sample holding the FM behavior state when finely tuning the Sb-doping content at around $x = 0.3$, but the Sb substitution undoubtedly weakens the SOC compared with the pure $\mathrm{MnBi_4Te_7}$, in which a topological transition may occur. Thus, further identification of the topological nature of this FM sample of $\mathrm{Mn(Bi_{0.7}Sb_{0.3})_4Te_7}$ is essential. In Figs. 3(a)–3(f), ARPES results of $\mathrm{Mn(Bi_{0.7}Sb_{0.3})_4Te_7}$ ($\mathrm{Bi_2Te_3}$ termination) at the photon energies from 7.25 to 23 eV are displayed. It is obvious to distinguish a linear dispersion which is independent of the photon energies. Comparing with the previous reports [36,37], we find that, regardless of the different Fermi energy, the dispersions of $\mathrm{Mn(Bi_{0.7}Sb_{0.3})_4Te_7}$ are almost like the ones of pure $\mathrm{MnBi_4Te_7}$, and the linear dispersions are identified as the topological surface states (marked by the arrows in Figs. 3(a)–3(f). Therefore, by ARPES measurement, it is confirmed that the nontrivial topological property is still retentive in $\mathrm{Mn(Bi_{0.7}Sb_{0.3})_4Te_7}$. The surface Dirac cone shows the nongap feature which may be attributed to the modified hybridization between topological surface state and the valence bands after Sb doping [33,42]. Comparing with the pure $\mathrm{MnBi_4Te_7}$ (~0.3 eV), the Dirac point is much closer to the Fermi level in $\mathrm{Mn(Bi_{0.7}Sb_{0.3})_4Te_7}$, ~0.22 eV. The tendency of the Fermi level descending indicates the relative low carrier density in $x = 0.3$.

Accompanied by the engineering of the magnetism, Sb doping can also modify the carrier density of $\mathrm{MnBi_4Te_7}$. Due to the internal defects of Mn and Bi antisites, the as-grown $\mathrm{MnBi_2Te_4}$ and related heterostructure $\mathrm{MnBi_4Te_7}$ are serious n-type doped regardless of the growth methods [14,22]. Heavy bulk carriers will obstruct the regulating capacity of the gate voltage which confines the device experiments to ultrathin films. According to previous efforts in topological insulators [27,43], antimony dopant is efficient to adjust the Fermi level and to induce p-type doping without destructing the topological property and the carrier mobility in the TI samples. The magnetoresistivity and Hall resistivity of $\mathrm{Mn(Bi_{1-x}Sb_x)_4Te_7}$ are shown in Fig. 4. In Fig. 4(c), the carrier densities are extracted from the Hall resistivity at 20 K. One can find that the $n - p$ transition occurs at the ratio between $x = 0.36$ and 0.4, in which the sign of the Hall coefficient changes from negative to positive, and the extracted carrier densities in $x = 0.36$ and 0.4 are $1.65 \times 10^{19}\ \mathrm{cm^{-3}}$ (n type) and $2.6 \times 10^{19}\mathrm{cm^{-3}}$ (p type), respectively, 10 times smaller than the value in pure $\mathrm{MnBi_4Te_7}$. Since the charge neutrality point has been verified,

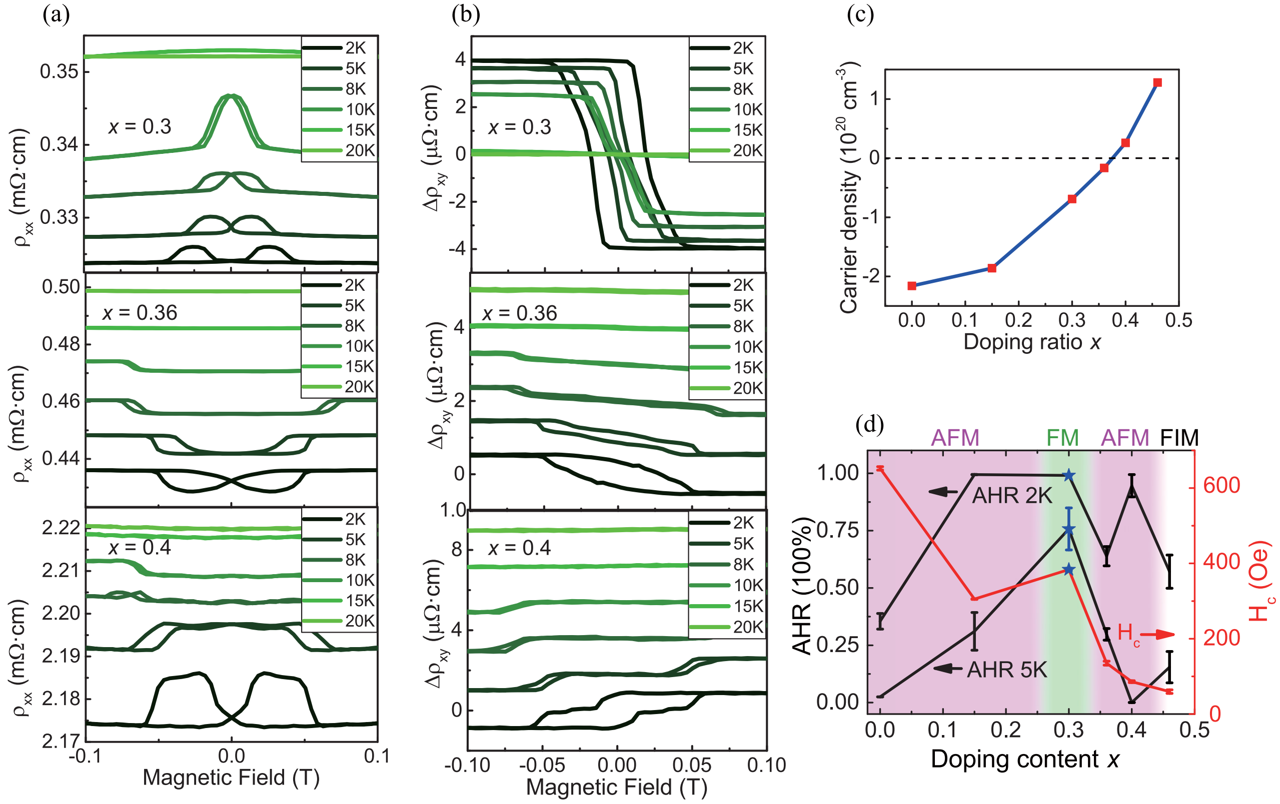

FIG. 4. Electrical transport and the evolution diagram of $\mathrm{Mn(Bi_{1-x}Sb_x)_4Te_7}$ under H//c. (a) Magneto resistivity and (b) the anomalous Hall after subtracting the background at the selected ratios: $x = 0.3$, 0.36, and 0.4. The curves of $x = 0.36$ and 0.4 are offset for clarity. (c) Carrier densities extracted from the Hall signals at 20 K. (d) Anomalous Hall effect (AHE) ratio at 2 and 5 K and the coercive field of the samples. The background colors represent the antiferromagnetic (AFM), ferromagnetic (FM), and ferrimagnetic region.

we then pay more attention to the magnetotransport behavior of the samples which are near the charge neutrality point. In Figs. 4(a) and 4(b), the longitudinal and transverse resistivity show clear butterfly curves and hysteresis loops due to the spontaneous magnetization. Because of the complex magnetic competition between the AFM and FM states, the resistivity vs magnetic field curves display the complex evolution trend near the neutrality point from $x = 0.3$ to 0.4. It is worth noting that the Hall signal changes the sign from $x = 0.3$ to 0.46. Similar results have been discovered in $\mathrm{MnBi_2Te_4}$, which are believed to be attributed to the competition of intrinsic Berry curvature and extrinsic skew scattering [44]. The AHE of $x = 0.36$ displays a queer behavior with round-shaped loops, probably because it is close to the transition point from negative to positive AHE. Like with the *M-H* curves, the hysteresis loop of the Hall resistivity separates into two individual loops when the temperature rises to 8 K, except the $\mathrm{Mn(Bi_{0.7}Sb_{0.3})_4Te_7}$ sample. In $\mathrm{Mn(Bi_{0.7}Sb_{0.3})_4Te_7}$ with the FM behavior state, the AHE is still observable near the zero field at 8 and 10 K, corresponding to the hysteresis loop in *M-H* signals. Contrary to stubborn AFM in Sb-doped $\mathrm{MnBi_2Te_4}$ [26,27], it is apparent that the FM behavior state can be approached accompanied with the successful modulation of carrier densities in Sb-doped $\mathrm{MnBi_4Te_7}$ samples. To show and elucidate the evolution of the magnetism and the electrical transport during the procedure of doping, we summarize the anomalous Hall ratio (AHR) at zero field which is defined as $[\rho_{\mathrm{AHE}}(0T)]/[\rho_{\mathrm{AHE}}(\text{saturation field: 0.3 T for } x = 0 \text{ and 0.1 T for the other ratios})]$ as well as the coercive field of the six samples in the diagram displayed in Fig. 4(d). Compared with the pure $\mathrm{MnBi_4Te_7}$ sample (~0.066 T), the coercive fields decrease monotonically after doping, except an obvious peak at $\mathrm{Mn(Bi_{0.7}Sb_{0.3})_4Te_7}$. However, on the contrary, the AHE ratio enhances dramatically under antimony substitution. For the AHR, it is only ~25% at 2 K and decreases to ~0% at 5 K in pure $\mathrm{MnBi_4Te_7}$ with an AFM ground state. In the sample of $x = 0.15$, AHR rises to ~100% at 2 K but quickly decreases to ~30%. In contrast, due to the FM behavior state with magnetic polarization under zero field in $\mathrm{Mn(Bi_{0.7}Sb_{0.3})_4Te_7}$, the AHR at zero field can not only hold at ~100% at the low temperature of 2 K, but also preserves at ~75% at a higher temperature of 5 K, which is the largest AHR comparing with the samples with other doping ratios from 0 to 0.46. It is obvious that the AFM [pink background in Fig. 4(d)] transforming to FM in $\mathrm{Mn(Bi_{0.7}Sb_{0.3})_4Te_7}$ [pale green background zone in Fig. 4(d)], with the abnormal high coercive field and AHR, ensures strong spontaneous magnetization at zero field and would be favorable for further device fabrication and related studies on magnetism modulation, QAHE, and other expected phenomena.

By magnetism and transport measurements, the attractive combination between FM and topology in $\mathrm{Mn(Bi_{0.7}Sb_{0.3})_4Te_7}$ has been experimentally demonstrated, but the mechanism behind it is still unclear and needs to be further theoretically

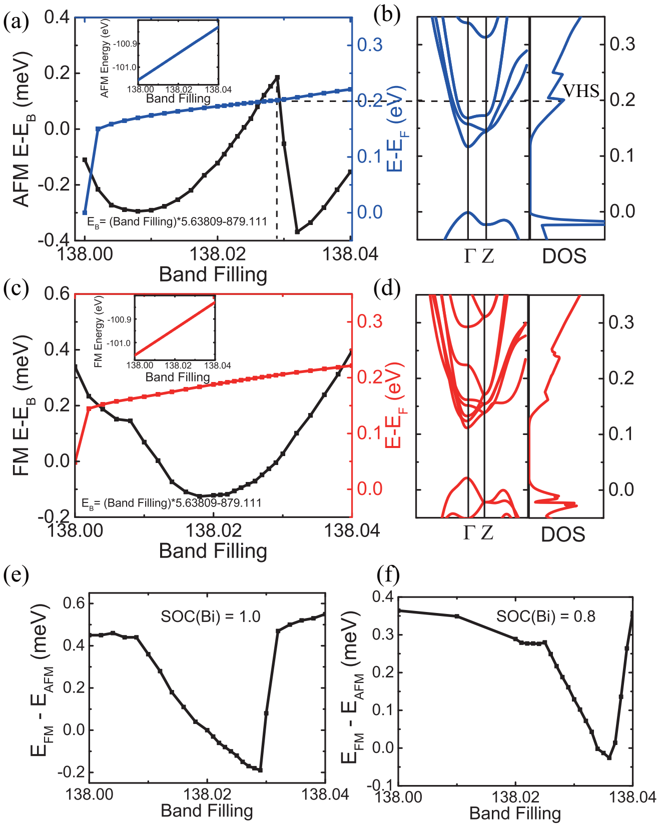

FIG. 5. The energy differences and the electronic structures between the antiferromagnetic (AFM) and ferromagnetic (FM) states in $\mathrm{Mn(Bi_{1-x}Sb_x)_4Te_7}$. (a) The energy of the AFM state after subtracting the linear background. Inset: The original data of the AFM energy. (b) The band structures and the related density of states (DOS) for the AFM state. (c) and (d) The energy, band structure, and the DOS for the FM state. (e) and (f) Energy differences of FM-AFM at the spin-orbit coupling (SOC) = 1.0 and 0.8, respectively. The black dashed lines show the exact position of the Van Hove singularity (VHS). The zero point of the $E - E_F$ is set at the Dirac point of the surface state.

revealed. Using first-principles calculations, it is confirmed that the band accidentally filling a VHS may play an important role here. The magnetism transition due to the abrupt change of the density of states (DOS) like the VHS has been studied by many researchers [45–47]. The abrupt changes of the DOS will induce the VHS. Due to the emergence of the VHS, the magnetism will be changed. For feasibility, we change the electron numbers N in the unit cell to simulate the realistic band filling. In Figs. 5(a) and 5(c), we plot the energy of the AFM and FM states, respectively, after subtracting the linear background $E_B = (\text{bandfilling}) \times 5.63809-879.111$. The energy of the AFM state increases sharply ∼138.03. However, for the FM state, the energy rises gently without violent changes. In this case, the energy difference of the FM-AFM will display a nonmonotonic dip. To explain the unusual increase of the AFM state, we calculate the band structure and the related DOS in Figs. 5(b) and 5(d). For the AFM state, when the Fermi level moves ∼0.21 eV, the DOS approaches the jump point, described as the VHS (marked by the black dashed lines). Large degeneracy of the DOS at this VHS causes the AFM to be unstable, transforming the system into a FM phase. Near the VHS, the energy of the AFM exceeds the one of the FM state, inducing the narrow region of the FM ground state. Specifically, as is shown in Fig. 5(e), the energy difference between the FM and AFM phases ΔE is positive at $N = 138$ with the Fermi level in the band gap, which indicates the AFM ground state dominates the whole magnetism. When increasing the N value, the Fermi energy rises to the conduction band, while the energy difference slowly decreases. When $N = 138.029$, which is close to the VHS, the ΔE turns negative, and the system evolves into a FM ground state. Intriguingly, the Fermi energy of the VHS is 0.21 eV higher than the valance band in the FM ground state, close to the Fermi level of the $\mathrm{Mn(Bi_{0.7}Sb_{0.3})_4Te_7}$ FM behavior sample which is verified by ARPES. When N continues to increase, the ΔE rises quickly, and the system returns to the AFM state. Furthermore, to consider the 30% antimony doping effect, we reduced the SOC strength of the Bi atoms to 0.8 of the original value. As is shown in Figs. 5(f), the VHS corresponding to the FM state is also clear and retained at 0.25 eV above the valance band. Integrated calculated results with SOC(Bi) = 0.8 are displayed in Fig. S2 in the Supplemental Material [41]. Overall, the accidental VHS at nearly $x = 0.3$ results in the nonmonotonic magnetic transition and the exotic FM region. Except for the influence of the SOC after Sb doping, we also consider the changes of the unit cell volume and the Mn-Bi antisite. In pure $\mathrm{MnBi_2Te_4}$ and $\mathrm{MnBi_4Te_7}$, antisite defects between Mn and Bi atoms are believed to exist [14,22,48]. Upon increasing the ratio of the Mn-Bi antisite, the FM-AFM energy difference will decrease directly. However, according to the theoretical calculation, the Mn-Bi antisite only shows monotonic effects to the FM-AFM energy differences which will not induce the nonmonotonic AFM-FM-AFM magnetic transitions at the samples near $x = 0.3$. Along with the further increase of the Sb-doping ratio, the influence of the Mn-Sb defects will enhance, which may be the origin of the emergence of the ferrimagnetism at $x = 0.46$ [49–51]. Furthermore, under different unit cell volumes, the FM-AFM energy difference still possesses a similar dip near $x = 0.3$, indicating the authenticity of the unique FM region. Overall, we consider the unit cell volume, SOC, and the Mn-Bi antisite in the theoretical calculations. The value of the dip strongly depends on the specific computational parameters. Based on the theoretical calculations, it is hard to estimate whether the dip drops to the negative value, which determines the ground state of $\mathrm{Mn(Bi_{0.7}Sb_{0.3})_4Te_7}$. However, combining the results of the theoretical calculations and the experiments, we think the FM behavior state is possible and reliable in the actual situation. We believe that the theoretical calculation is reasonable, which corresponds with the experimental results very well.

IV. CONCLUSIONS

In summary, the magnetism and the carrier density have been modulated simultaneously in $\mathrm{Mn(Bi_{1-x}Sb_x)_4Te_7}$ single crystals. The AFM ground state evolves to the FM behavior state at $x = 0.3$ and then returns to AFM at $x = 0.36$. Multiple interactions including carrier densities, SOC, FM-AFM coupling, and Mn-Sb antisites involve and contribute to the total magnetism. The ARPES results clearly display the existence of topological surface states of $\mathrm{Mn(Bi_{0.7}Sb_{0.3})_4Te_7}$ with the FM behavior state, confirming the coexistence of FM and topology in this sample. Additionally, the charge carriers can be modified, and an $n-p$ carrier transition occurs at $x = 0.3$–0.4, where intriguing magnetic and charge carrier transitions occur, providing an excellent avenue to study the coupling between the magnetism and carriers. $\mathrm{Mn(Bi_{0.7}Sb_{0.3})_4Te_7}$ is a promising candidate of a MTI with the FM behavior state and low bulk carrier concentration. This material displays an improved performance of both magnetism and electrical transport compared with pure $\mathrm{MnBi_4Te_7}$. Our results shed light on the exploration of the intrinsic MTI candidates and research on modulating the topology, magnetism, and charge carriers simultaneously in magnetic topological materials.

ACKNOWLEDGMENTS

The authors gratefully acknowledge the financial support of the National Key R&D Program of China (No. 2017YFA0303203 and No. 2016YFA0300204), the National Natural Science Foundation of China (Grant No. 12025404, No. 91622115, No. 11522432, No. 11574217, No. U1732273, No. U1732159, No. 61822403, No. 11874203, No. 11904165, No. 11904166, No. 11674165, and No. 11227902), the Natural Science Foundation of Jiangsu Province (No. BK20190286 and No. BK20200007), the Users with Excellence Program of Hefei Science Center Chinese Academy of Sciences (CAS; No. 2019HSC-UE007), the Fundamental Research Funds for the Central Universities (No. 020414380082, No. 020414380194, and No. 020414380038), the opening Project of the Wuhan National High Magnetic Field Center, the Fok Ying-Tong Education Foundation of China (No. 161006), the High-Performance Computing Center of Collaborative Innovation Center of Advanced Microstructures, and the Award for Outstanding Member in Youth Innovation Promotion Association CAS.

B.C, D.W., Z.J., and B.Z. contributed equally to this Work.

---

[1] R. Yu, W. Zhang, H.-J. Zhang, S.-C. Zhang, X. Dai, and Z. Fang, Science **329**, 61 (2010).

[2] C.-Z. Chang, J. Zhang, X. Feng, J. Shen, Z. Zhang, M. Guo, K. Li, Y. Ou, P. Wei, L.-L. Wang, Z.-Q. Ji, Y. Feng, S. Ji, X. Chen, J. Jia, X. Dai, Z. Fang, S.-C. Zhang, K. He, Y. Wang, L. Lu, X.-C. Ma, and Q.-K. Xue, Science **340**, 167 (2013).

[3] K. He, Y. Wang, and Q.-K. Xue, Natl. Sci. Rev. **1**, 38 (2014).

[4] C.-X. Liu, S.-C. Zhang, and X.-L. Qi, Annu. Rev. Condens. Matter Phys. **7**, 301 (2016).

[5] K. Nomura and N. Nagaosa, Phys. Rev. Lett. **106**, 166802 (2011).

[6] R. Li, J. Wang, X.-L. Qi, and S.-C. Zhang, Nat. Phys. **6**, 284 (2010).

[7] D. W. Jinlong Zhang, M. Shi, T. Zhu, H. Zhang, J. Wang, Chin. Phys. Lett. **37**, 077304 (2020).

[8] M. Mogi, R. Yoshimi, A. Tsukazaki, K. Yasuda, Y. Kozuka, K. S. Takahashi, M. Kawasaki, and Y. Tokura, Appl. Phys. Lett. **107**, 182401 (2015).

[9] C.-Z. Chang, W. Zhao, D. Y. Kim, H. Zhang, B. A. Assaf, D. Heiman, S.-C. Zhang, C. Liu, M. H. W. Chan, and J. S. Moodera, Nat. Mater. **14**, 473 (2015).

[10] M. Lang, M. Montazeri, M. C. Onbasli, X. Kou, Y. Fan, P. Upadhyaya, K. Yao, F. Liu, Y. Jiang, W. Jiang, K. L. Wong, G. Yu, J. Tang, T. Nie, L. He, R. N. Schwartz, Y. Wang, C. A. Ross, and K. L. Wang, Nano Lett. **14**, 3459 (2014).

[11] Y. Ou, C. Liu, G. Jiang, Y. Feng, D. Zhao, W. Wu, X.-X. Wang, W. Li, C. Song, L.-L. Wang, W. Wang, W. Wu, Y. Wang, K. He, X.-C. Ma, and Q.-K. Xue, Adv. Mater. **30**, 1703062 (2018).

[12] D. Zhang, M. Shi, T. Zhu, D. Xing, H. Zhang, and J. Wang, Phys. Rev. Lett. **122**, 206401 (2019).

[13] J. Li, Y. Li, S. Du, Z. Wang, B.-L. Gu, S.-C. Zhang, K. He, W. Duan, and Y. Xu, Sci. Adv. **5**, eaaw5685 (2019).

[14] M. M. Otrokov *et al.*, Nature (London) **576**, 416 (2019).

[15] M. M. Otrokov, I. P. Rusinov, M. Blanco-Rey, M. Hoffmann, A. Y. Vyazovskaya, S. V. Eremeev, A. Ernst, P. M. Echenique, A. Arnau, and E. V. Chulkov, Phys. Rev. Lett. **122**, 107202 (2019).

[16] Y. Gong, J. Guo, J. Li, K. Zhu, M. Liao, X. Liu, Q. Zhang, L. Gu, L. Tang, and X. Feng, Chin. Phys. Lett. **36**, 076801 (2019).

[17] Y.-J. Hao, P. Liu, Y. Feng, X.-M. Ma, E. F. Schwier, M. Arita, S. Kumar, C. Hu, R. e. Lu, M. Zeng, Y. Wang, Z. Hao, H.-Y. Sun, K. Zhang, J. Mei, N. Ni, L. Wu, K. Shimada, C. Chen, Q. Liu, and C. Liu, Phys. Rev. X **9**, 041038 (2019).

[18] Y. J. Chen, L. X. Xu, J. H. Li, Y. W. Li, H. Y. Wang, C. F. Zhang, H. Li, Y. Wu, A. J. Liang, C. Chen, S. W. Jung, C. Cacho, Y. H. Mao, S. Liu, M. X. Wang, Y. F. Guo, Y. Xu, Z. K. Liu, L. X. Yang, and Y. L. Chen, Phys. Rev. X **9**, 041040 (2019).

[19] Y. X. Cuiying Pei, J. Wu, Y. i. Zhao, L. Gao, T. Ying, B. o. Gao, N. Li, W. Yang, D. Zhang, H. Gou, Y. Chen, H. Hosono, G. Li, and Y. Qi, Chin. Phys. Lett. **37**, 066401 (2020).

[20] H. Sun, B. Xia, Z. Chen, Y. Zhang, P. Liu, Q. Yao, H. Tang, Y. Zhao, H. Xu, and Q. Liu, Phys. Rev. Lett. **123**, 096401 (2019).

[21] J. Wu, F. Liu, M. Sasase, K. Ienaga, Y. Obata, R. Yukawa, K. Horiba, H. Kumigashira, S. Okuma, T. Inoshita, and H. Hosono, Sci. Adv. **5**, eaax9989 (2019).

[22] J. Q. Yan, Q. Zhang, T. Heitmann, Z. Huang, K. Y. Chen, J. G. Cheng, W. Wu, D. Vaknin, B. C. Sales, and R. J. McQueeney, Phys. Rev. Materials **3**, 064202 (2019).

[23] Y. Deng, Y. Yu, M. Z. Shi, Z. Guo, Z. Xu, J. Wang, X. H. Chen, and Y. Zhang, Science **367**, 895 (2020).

[24] C. Liu, Y. Wang, H. Li, Y. Wu, Y. Li, J. Li, K. He, Y. Xu, J. Zhang, and Y. Wang, Nat. Mater. **19**, 522 (2020).

[25] J. Ge, Y. Liu, J. Li, H. Li, T. Luo, Y. Wu, Y. Xu, and J. Wang, Natl. Sci. Rev. **7**, 1280 (2020).

[26] B. Chen *et al.*, Nat. Commun. **10**, 4469 (2019).

[27] J. Q. Yan, S. Okamoto, M. A. McGuire, A. F. May, R. J. McQueeney, and B. C. Sales, Phys. Rev. B **100**, 104409 (2019).

[28] X.-M. Ma *et al.*, Phys. Rev. B **103**, L121112 (2021).

[29] G. Kresse and J. Hafner, Phys. Rev. B **47**, 558 (1993).

[30] G. Kresse and D. Joubert, Phys. Rev. B **59**, 1758 (1999).

[31] L. Ding, C. Hu, F. Ye, E. Feng, N. Ni, and H. Cao, Phys. Rev. B **101**, 020412(R) (2020).

[32] J. Q. Yan, Y. H. Liu, D. S. Parker, Y. Wu, A. A. Aczel, M. Matsuda, M. A. McGuire, and B. C. Sales, Phys. Rev. Mater. **4**, 054202 (2020).

[33] I. I. Klimovskikh *et al.*, npj Quantum Mater. **5**, 54 (2020).

[34] Y. Hu, L. Xu, M. Shi, A. Luo, S. Peng, Z. Y. Wang, J. J. Ying, T. Wu, Z. K. Liu, C. F. Zhang, Y. L. Chen, G. Xu, X.-H. Chen, and J.-F. He, Phys. Rev. B **101**, 161113(R) (2020).

[35] H. Li *et al.*, Phys. Rev. X **9**, 041039 (2019).

[36] C. Hu, K. N. Gordon, P. Liu, J. Liu, X. Zhou, P. Hao, D. Narayan, E. Emmanouilidou, H. Sun, Y. Liu, H. Brawer, A. P. Ramirez, L. Ding, H. Cao, Q. Liu, D. Dessau, and N. Ni, Nat. Commun. **11**, 97 (2020).

[37] R. C. Vidal *et al.*, Phys. Rev. X **9**, 041065 (2019).

[38] X. Wu *et al.*, Phys. Rev. X **10**, 031013 (2020).

[39] M. Z. Shi, B. Lei, C. S. Zhu, D. H. Ma, J. H. Cui, Z. L. Sun, J. J. Ying, and X. H. Chen, Phys. Rev. B **100**, 155144 (2019).

[40] H. Xie, D. Wang, Z. Cai, B. Chen, J. Guo, M. Naveed, S. Zhang, M. Zhang, X. Wang, F. Fei, H. Zhang, and F. Song, Appl. Phys. Lett. **116**, 221902 (2020).

[41] See Supplemental Material at http://link.aps.org/supplemental/10.1103/PhysRevB.104.075134 for the magnetism measurements of the other four FM-behavior samples and the additional theoretical calculations of the FM-AFM energy difference.

[42] R. C. Vidal, H. Bentmann, J. I. Facio, T. Heider, P. Kagerer, C. I. Fornari, T. R. F. Peixoto, T. Figgemeier, S. Jung, C. Cacho, B. Büchner, J. van den Brink, C. M. Schneider, L. Plucinski, E. F. Schwier, K. Shimada, M. Richter, A. Isaeva, and F. Reinert, Phys. Rev. Lett. **126**, 176403 (2021).

[43] T. Arakane, T. Sato, S. Souma, K. Kosaka, K. Nakayama, M. Komatsu, T. Takahashi, Z. Ren, K. Segawa, and Y. Ando, Nat. Commun. **3**, 636 (2012).

[44] S. Zhang, R. Wang, X. Wang, B. Wei, B. Chen, H. Wang, G. Shi, F. Wang, B. Jia, Y. Ouyang, F. Xie, F. Fei, M. Zhang, X. Wang, D. Wu, X. Wan, F. Song, H. Zhang, and B. Wang, Nano Lett. **20**, 709 (2020).

[45] M. Fleck, A. M. Oleś, and L. Hedin, Phys. Rev. B **56**, 3159 (1997).

[46] W. F. Goh and W. E. Pickett, Europhys. Lett. **116**, 27004 (2016).

[47] C.-W. Wu, J.-H. Huang, and D.-X. Yao, J. Magn. Magn. Mater. **469**, 306 (2019).

[48] S. H. Lee, Y. Zhu, Y. Wang, L. Miao, T. Pillsbury, H. Yi, S. Kempinger, J. Hu, C. A. Heikes, P. Quarterman, W. Ratcliff, J. A. Borchers, H. Zhang, X. Ke, D. Graf, N. Alem, C.-Z. Chang, N. Samarth, and Z. Mao, Phys. Rev. Research **1**, 012011(R) (2019).

[49] C. Hu, S.-W. Lien, E. Feng, S. Mackey, H.-J. Tien, I. I. Mazin, H. Cao, T.-R. Chang, and N. Ni, arXiv:2008.09097.

[50] Y. Liu, L.-L. Wang, Q. Zheng, Z. Huang, X. Wang, M. Chi, Y. Wu, B. C. Chakoumakos, M. A. McGuire, B. C. Sales, W. Wu, and J. Yan, Phys. Rev. X **11**, 021033 (2021).

[51] T. Murakami, Y. Nambu, T. Koretsune, G. Xiangyu, T. Yamamoto, C. M. Brown, and H. Kageyama, Phys. Rev. B **100**, 195103 (2019).